Design and optimization of cancellation coil topologies for a ferrite-less wireless EV charging pad

Aaron D. Scher, Mostak Mohammad*, Burak Ozpineci*, Omer Onar*
Department of Electrical Engineering and Renewable Energy, Oregon Institute of Technology, Wilsonville, OR 97070, USA
*Building and Transportation Research Division, Oak Ridge National Laboratory, National Transportation Research Center, Knoxville, TN 37932, USA
Email: aaron.scher@oit.edu, mohammadm@ornl.gov, burak@ornl.gov, onaroc@ornl.gov

***Abstract*- Ferrite cores are widely used in conventional wireless EV charging pads to reduce stray EMF emissions, but they can be brittle, heavy, and expensive. This work furthers the development of ferrite-less wireless charging pads by comparing an active and two distinct passive cancellation coil topologies as candidates to replace the ferrite. Using the software packages FEMM and MATLAB, each topology is optimized to find the best winding positions and radii to minimize leakage at a specified position under the side of the vehicle. The optimized designs are compared for shielding effectiveness, induced current, and efficiency. All three topologies are able to sufficiently reduce the leakage field below the ICNIRP limit of 27 μT_{rms} with just one turn. Interestingly, we find that an array of simple passive cancellation loops performs similar to the more widely studied passive cancellation coil.**

I. Introduction

Wireless power transfer (WPT) technology is a leading solution for streamlining the electric vehicle (EV) charging experience [1]. In a typical stationary wireless charging scenario, the EV is parked over a special parking space outfitted with a transmitter embedded under or on the ground surface, as shown in Fig. 1. The transmitter contains a primary coil that transfers power via magnetic induction to a secondary coil located under the vehicle. By removing the need to physically connect a charging cable between the charging station and EV, a wireless charging system (WCS) offers convenience for drivers and simplifies automated charging for autonomous EVs. The technology is maturing and ready for adoption as the Society of Automotive Engineers (SAE) has released the standard for wireless charging systems ranging from 3.7 kW to 11 kW [2], [3]. Looking forward, dynamic WPT technology shows potential to ease battery capacity requirements by allowing EVs to charge while driving over charging lanes [4].

This manuscript has been authored by Oak Ridge National Laboratory, operated by UT-Battelle, LLC, under Contract No. DE-AC05-00OR22725 with the U.S. Department of Energy. The United States Government retains and the publisher, by accepting the article for publication, acknowledges that the United States Government retains a non-exclusive, paid-up, irrevocable, world-wide license to publish or reproduce the published form of this manuscript, or allow others to do so, for United States Government purposes. The Department of Energy will provide public access to these results of federally sponsored research in accordance with the DOE Public Access Plan (http://energy.gov/downloads/doe-public-access-plan).

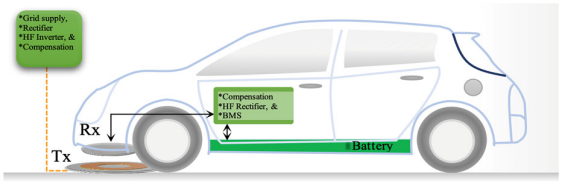

Fig. 1. Diagram of the wireless charging system for EVs.

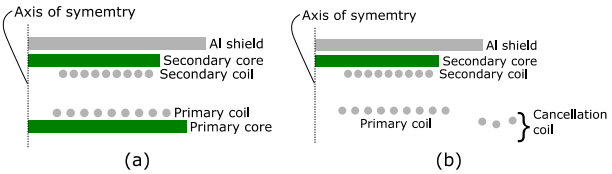

Fig. 2. Magnetic coupler (a) with a conventional primary core and (b) with a ferrite-less charging pad using a cancellation coil.

Unipolar circular and rectangular pads are two of the most common charging pad topologies for high power EV-charging. The radially cross-sectional view of an axisymmetric transmitter and receiver pads are shown in Fig. 2. The charging pads contain a planar ferrite core under the transmit coil, like that included in the simplified magnetic coupler depicted in Fig. 2 (a). The primary core provides a low reluctance path for the magnetic flux and also shields the surrounding area by guiding the magnetic flux within a confined space near the charging pad. While simple and effective, the core also has disadvantages in that it can be brittle, heavy, and expensive. This has prompted researchers to pursue ferrite-less designs [5]–[10]. A key challenge with a ferrite-less system is that it can generate higher magnetic field emissions compared to a traditional ferrite-based design. To suppress the increased magnetic field emission, in the literature, shielding is achieved by driving or inducing conduction currents whose fields oppose the applied fields [5], [9]. Planar coils and loops are well-suited for shielding as they are simple and robust and can exhibit low loss if implemented with Litz wire [11], [12]. Fig. 2 (b) shows a modified magnetic coupler with a ferrite-less charging pad that includes a passive three-turn cancellation coil to provide shielding. However, many Litz-wire based shields for ferrite-less systems are designed with active-excitation, keeping the coils in close proximity of the main

coils, which is highly nonoptimal, causing higher loss, reducing mutual inductance, requiring higher current in the shield, and increasing the thickness of the required Litz wire.

In this paper, three different types of Litz-wire based shield topologies are designed and optimized: passive independent shield loops, passive series-connected loops, and an active shield. The optimal shield topology and optimal position of the shield coils are designed to minimize stray EMF emmissions while requiring low shield current and minimal impact on the power transfer efficiency. To the best of the authors' knowledge, this paper presents the first optimization-based comparative analysis for all three Litz-wire based shield topologies under consideration.

II. Methodology

A. Problem setup

This work focuses on the design of Litz-wire based shields for a ferrite-less 11 kW wireless EV charging pad. The airgap between the coils is 140 mm, the transmit frequency is 85 kHz, and the output power is 11 kW. Unipolar circular primary and secondary pads are considered for simplicity and to allow for rapid axisymmetric 2D FEA-based optimizaiton of the shields. For rectangular geometries, a subsequent 3D FEA-based optimization can be performed with comparable rectangular coils to fine-tune the design.

Fig. 3 illustrates three distinct cancellation coil topologies considered for limiting EMF emissions. The black spiral is the primary driver coil, and the outer red turns constitute the cancellation coil or loop array shield. Fig. 3 (a) shows a two-turn passive cancellation loop array, Fig. 3 (b) shows a two-turn passive cancellation coil, and Fig. 3 (c) shows a two-turn active cancellation coil driven in an opposing sense to the main primary coil. The shielding effectiveness of the passive and active cancellation coils shown in Fig. 3 (b) and (c) are better known, but there has not been an optimization-based comparative analysis for of all three configurations. Our approach is to optimize each design by finding the best winding positions and radii to minimize leakage magnetic field, and then compare the performances of the optimized designs in terms of shielding effectiveness, induced current amplitude, and coil-to-coil efficiency.

By convention, the geometry is assumed axisymmetric about the z-axis and the primary coil is located on the $z = 0$ plane. Following the guideline set by SAE J2954, the goal is to minimize EMF emissions at position $P(r, z) =$ (800 mm, 75 mm), which is directly beneath the side of the vehicle where people may be exposed. For reference, Fig. 4 (a) shows a flux density plot generated using FEMM [13] (a popular FEA software package) for a traditional WCS with a primary ferrite. Pad designs are comparable with the SAE J2954 WPT3/Z2 reference designs. The computed inductances of the circular primary and secondary coils are 53.0 μH and 44.5 μH, respectively, which are similar to the inductances reported for comparable rectangular designs [14]. For this simulation, the battery voltage and current are V_{bat} = 330 V and $I_{bat} = P_{bat}/V_{bat} = 33.33$ A, respecitively. For the simulation, AC voltages and currents are specified assuming a series-series componesated IPT at resonance with a full-bridge inverter and full-wave rectifier.

Note that a top aluminum (Al) plate is included to model the shield under the vehicle chassis. The vehicle chassis itself could be modeled by a steel plate above the top Al plate. However, this structure is not included in our simulations for simplicity and to make clear how removing the ferrite increases the field above the top Al plate.

In Fig. 4 (a) the "X" mark is placed at position $P(r, z) =$ (800 mm, 75 mm) and the magnetic flux density at this position is 6.22 μT_{rms}, which is well-below the ICNIRP limit of 27 μT_{rms} [15]. Fig. 4 (b) shows the resulting flux density plot if we remove the primary pad's ferrite and Al backplate. Here we assume a scenerio in which shielding is not necessary below the primary. Removing the ferrite decreases the self and mutual inductances. To offset this effect, we make the primary a two-layer coil. As Fig. 4 (b) shows, the flux leakage at position $P(r, z) =$ (800 mm, 75 mm) for the ferrite-less transmitter is 25.63 μT_{rms} which is very close to 27 μT_{rms}. The increased leakage magnetic field necessitates additional shielding for the ferrite-less WCS. Table I provides the component parameter values of the secondary and ferrite-less primary pads.

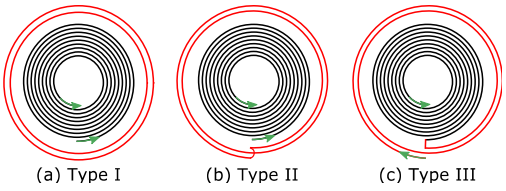

Fig. 3. Illustration (top-down view) of the three coil shield topology types considered in this study: (a) Type I: passive cancellation loop array, (b) Type II: passive cancellation coil, and (c) Type III: active cancellation coil.

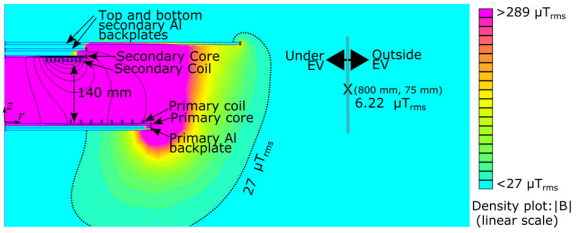

(a)

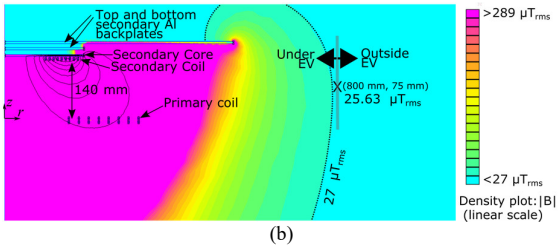

(b)

Fig. 4. Flux density plots of the magnetic coupler (a) with the primary core and (b) without the primary core (ferrite-less).

TABLE I
PARAMETER VALUES FOR WCS WITH FERRITE-LESS CHARGING PAD

Component or parameter	Parameter values
Al plate 2 (secondary)	Radius: 550 mm Thickenss: 5 mm
Air gap: Al plate 1 to Al plate 2	Air gap (top surface of Al plate 1 to bottom surface of Al plate 2): 10 mm
Al plate 1 (secondary)	Radius: 191 mm Thickenss: 5 mm
Air gap: RX core to Al plate 1	Air gap (RX core's top surface to bottom surface of Al plate 1): 11 mm
Rx core (secondary)	Magnetic permeability: $\mu_r = 3000$ Inner/outer radius: 0 mm/191 mm Thickness: 5 mm
Air gap: RX coil to core	Air gap (RX wire's top surface to RX core's bottom surface): 3 mm
Rx coil winding (secondary)	Material: Litz wire (2.5 mm wire radius) Winding type: single layer, unipolar, circular Number of turns: 9 Inner/outer radius (to wire center): 98.5 mm/176 mm
Air gap: RX to TX windings	Air gap (TX wire's top surface to RX wire's bottom surface): 140 mm
Tx coil winding (primary)	Material: Litz wire (2.5 mm wire radius) Winding type: double layer, unipolar, circular Number of turns: 8 per layer (16 total) Gap between top and bottom layers (wire surface to surface): 4 mm Inner/outer radius (to wire center): 155 mm/322 mm

B. *Optimization Problem*

Each of the three shield types under consideration (illustrated in Fig. 3) is composed of indidual single-turn cancellation coils, and the shield type itself (i.e, Type I, II, or III) is defined by the particular way these turns are connected. For a given shield type, our goal is to minimize the leakage field by optimizing the sizes and placements of the invidual cancellation coils that comprise the shield. The general optimization setup and procedure is similar for all three shield types and described below.

A shield is composed of N_c individual cancellation coils, and the set of N_c cancellation coils is denoted $\mathbf{c} = \{c_1, c_2, \dots, c_{N_c}\}$. We define a radius vector $\mathbf{r}_c = \left[r_{c_1}, r_{c_1}, \dots, r_{c_{N_c}}\right]$ and z-position vector $\mathbf{z}_c = \left[z_{c_1}, z_{c_1}, \dots, z_{c_{N_c}}\right]$ which provide the values the radii and vertical z-positions of each cancellation coil, respectively. The goal of our optimization problem is to find $\mathbf{r}_c$ and $\mathbf{z}_c$ that minimizes the leakage field magntiude B_P at a given position $P(r, z)$, subject to a set of constraints.

The first constraint is that, with the exception of the cancellation coils' radii and z-positions, the physical and material properties of the magnetic design are fixed. The second constraint is that the load voltage V_{bat} and output power P_{bat} are fixed. Third, to ensure adequate coil-to-coil efficiency η, we impose the inequality constraint $\eta \geq \eta_{min}$, where η_{min} is a minimum allowable efficiency. Forth, the radii and vertical z-positions of the cancellation coils are constrained by the inequalities: $r_{min} \leq r_{c,i} \leq r_{max}$ and $z_{max} \leq z_{c,i} \leq z_{max}$, where $i = 1,2, \dots, N$. Here, r_{min} and r_{max} are minimum and maximum allowable radii, respectively; and z_{min} and z_{max} are minimum and maximum allowable vertical z-positions, respectively. For simplicity, we do not impose constraints on the induced shield currents. Nonetheless, the maximum shield current amplitudes are important as they determine the minimum allowable Litz wire thickness. Shield currents will be considered in a later section when comparing the merits of the optimized shield designs.

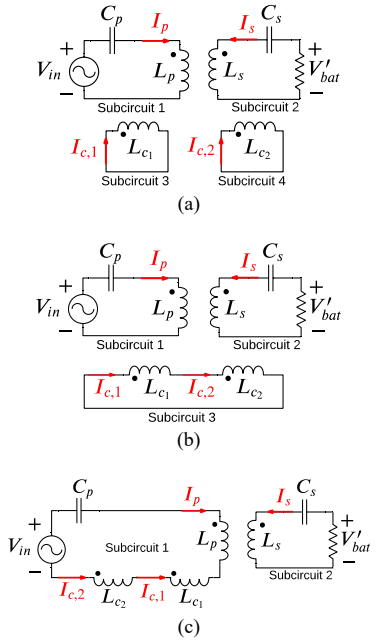

Fig. 5. Lumped element models of the WCS for the (a) Type I shield, (b) Type II shield, and (c) Type III shield. For this illustrated example, the shield is composed of two cancellation coils ($N_c = 2$).

C. *Magnetic analysis and modeling*

The section descibes the modelling and analysis of the WCS coupler. We define the model's input variables to be the radius and z-position vectors of the cancellation-coils ($\mathbf{r}_c$ and $\mathbf{z}_c$). The model's output variables are the leakage field B_P, coil-to-coil efficiency η, and shield currents. The analysis is perfomed using a two-stage computational approach. First, the magnetic problem is numerically solved using FEA with FEMM. Next, the numerical results are used to calculate the desired output variables by a sequence of computations with MATLAB.

For computational purposes, each of the primary, secondary, and N_c cancellation coils are analyzed as distinct lumped inductors. In this manner, the system contains a total of $N = N_c + 2$ inductors. In general, these inductors are wired together to form a total of S series-connected subcircuits, which are all magnetically coupled. Here, $S = N_c + 2 = N$ for the Type I shield (passive cancellation loop array), $S = 3$ for the Type II shield (passive cancellation coil), and $S = 2$ for the Type III shield (active cancellation coil). Fig 5 illustrates lumped element circuit models of the WCS for all three shield types assuming a shield with two cancellation coils ($N_c = 2$).

FEA with FEMM is used to find the $N \times N$ inductance matrix $\mathbf{M}$ which provides the self and mutual inductances between all the inductors in the system:

$$\mathbf{M} = \begin{bmatrix} L_p & M_{ps} & M_{pc_1} & \dots & M_{pc_{N_c}} \\ M_{sp} & L_s & M_{sc_1} & \dots & M_{sc_{N_c}} \\ M_{c_1p} & M_{c_1s} & L_{c_1} & \dots & M_{c_1c_{N_c}} \\ \vdots & \vdots & \vdots & \ddots & \vdots \\ M_{c_Np} & M_{c_Ns} & M_{c_Nc_1} & \dots & L_{c_{N_c}} \end{bmatrix}, \quad (1)$$

where subscripts p, s, and c_i refer to the primary (transmit), secondary (receive), and i^{th} cancellation coils, respectively. For example, the element L_{pp} refers to the self-inductance of the primary (p), M_{ps} refers to the mutual inductance between the primary (p) and secondary (s), and M_{pc_1} refers to the mutual inductance between the parmary (p) and cancellation coil c_1.

FEA with FEMM is also used to find the $1 \times N$ normalized B-field vectors $\widehat{\mathbf{B}}_r$, and $\widehat{\mathbf{B}}_z$. These vectors provide the r- and z-components of the leakage magnetic B-field at position $P(r, z)$ produced by each inductor in the system driven by an AC current with amplitude 1 A, while all other inductors are "turned off" (i.e., open circuited):

$$\widehat{\mathbf{B}}_r = \begin{bmatrix} \hat{B}_{r,p} & \hat{B}_{r,s} & \hat{B}_{r,c_1} & \dots & \hat{B}_{r,c_{N_c}} \end{bmatrix} \quad (2)$$

$$\widehat{\mathbf{B}}_z = \begin{bmatrix} \hat{B}_{z,p} & \hat{B}_{z,s} & \hat{B}_{z,c_1} & \dots & \hat{B}_{z,c_{N_c}} \end{bmatrix}. \quad (3)$$

After the FEA, a sequence of computations is performed with MATLAB to find B_P, η, and the system currents. Our computational approach is desribed as follows.

First, we define the $1 \times N$ current and voltage vectors $\mathbf{I}$ and $\mathbf{V}$, which quantify the current through and voltage across each inductor, respectively:

$$\mathbf{V} = \begin{bmatrix} V_p & V_s & V_{c_1} & \dots & V_{c_{N_c}} \end{bmatrix}, \quad (4)$$

$$\mathbf{I} = \begin{bmatrix} I_p & I_s & I_{c_1} & \dots & I_{c_{N_c}} \end{bmatrix}, \quad (5)$$

Next we define a $1 \times N$ resistance vector $\mathbf{R}$ which provides the series resistance of each inductor in the system:

$$\mathbf{R} = \begin{bmatrix} R_p & R_s & R_{c_1} & \dots & R_{c_{N_c}} \end{bmatrix}. \quad (6)$$

Elements of $\mathbf{R}$ are computed analytically as $R_i = R'_{Litz}\ell_i$, where ℓ_i is the known length of the inductor corresponding to the i^{th} element of $\mathbf{R}$ and R'_{Litz} is the known wire resistance per meter of the Litz wire; for example, $R_{c_1} = R'_{Litz}2\pi r_{c_1}$.

We also define a wiring matrix $\mathbf{W}$ which expresses how the N inductors are connected to form a total of S series-connected subcircuits. By definition, $\mathbf{W}$ contains S rows and N columns. Each row of $\mathbf{W}$ describes a distinct series-connected subcircuit. A row is formed by placing a 1,0, or -1 in each of the N column positions to specify the corresponding inductor's connection. A value of 1 represents a series connection, a 0 represents no connection (i.e., the corresponding inductor is not included in the subcircuit), and a -1 represents an anti-series connection in terms of the dot convention with respect to the polarity of the inductor with the lowest index in the subcircuit. By convention, columns 1 and 2 refer to the primary and secondary coils, respectively. Columns 3, 4, … N refer to the cancellation loops $c_1, c_2, \dots, c_{N_c}$, respectively. Given the above description, the Type I shield (passive cancellation loop array), Type II shield (passive cancellation coil), and Type III shield (active cancellation coil) are characterized by the following wiring matrices:

$$\mathbf{W} = \begin{bmatrix} 1 & 0 & 0 & \dots & 0 \\ 0 & 1 & 0 & \dots & 0 \\ 0 & 0 & 1 & \dots & 0 \\ \vdots & \vdots & \vdots & \ddots & \vdots \\ 0 & 0 & 0 & \dots & 1 \end{bmatrix}, \quad \text{(Type I)} \quad (7)$$

$$\mathbf{W} = \begin{bmatrix} 1 & 0 & 0 & 0 & \dots & 0 \\ 0 & 1 & 0 & 0 & \dots & 0 \\ 0 & 0 & 1 & 1 & \dots & 1 \end{bmatrix}, \quad \text{(Type II)} \quad (8)$$

$$\mathbf{W} = \begin{bmatrix} 1 & 0 & -1 & -1 & \dots & -1 \\ 0 & 1 & 0 & 0 & \dots & 0 \end{bmatrix}. \quad \text{(Type III)} \quad (9)$$

Furthermore, we define the $1 \times S$ subcircuit voltage vector $\mathbf{V}_W$ that quantifies the terminal voltages across each of the S series-connected subcircuits:

$$\begin{aligned} \mathbf{V}_W &= \begin{bmatrix} V_{W.1} & V_{W,2} & V_{W,3} & \dots & V_{W,S} \end{bmatrix} \\ &= \begin{bmatrix} V_{in} & V'_{bat} & 0 & \dots & 0 \end{bmatrix} \end{aligned} \quad (10)$$

where V_{in} is the AC equivalent voltage applied to the primary and V'_{bat} is the AC equivalent battery voltage (rectifier input voltage). For a full-bridge rectifier, $V'_{bat} = 4V_{bat}/\pi$, where V_{bat} is the battery (load) DC voltage. We also define the $1 \times S$ subcircuit current vector $\mathbf{I}_W$ that quantifies the currents through each of the S series-connected subcircuits:

$$\begin{aligned} \mathbf{I}_W &= \begin{bmatrix} I_{W.1} & I_{W,2} & I_{W,3} & \dots & I_{W,S} \end{bmatrix} \\ &= \begin{bmatrix} I_p & I_s & I_{W,3} & \dots & I_{W,S} \end{bmatrix}, \end{aligned} \quad (11)$$

where I_p is the primary current and $I_s = -2\,P_{bat}/V'_{bat}$ is the secondary current. The relationship between $\mathbf{I}$ and $\mathbf{I}_W$ is:

$$\mathbf{I}^{\mathrm{T}} = \mathbf{W}^{\mathrm{T}}\mathbf{I}_W^{\mathrm{T}}. \quad (12)$$

We define the $1 \times S$ capactive reactance array $\boldsymbol{X}_{C_W}$ that quantifies the reactances of the compensation capacitors connected in series with each of the S subcircuits:

$$\boldsymbol{X}_{C_W} = \begin{bmatrix} \dfrac{-1}{\omega C_p} & \dfrac{-1}{\omega C_s} & 0 & \dots & 0 \end{bmatrix}, \quad (13)$$

where C_p and C_s are the capacitances of the primary and secondary compensation capacitors, respectively.

The WCS's terminal AC voltages are related by the following impedance equation (derived from linear circuit analysis):

$$\mathbf{V}_W^{\mathrm{T}} - \mathrm{diag}\left(j\boldsymbol{X}_{C_W}\right)\mathbf{I}_W^{\mathrm{T}} = \boldsymbol{Z}_W\mathbf{I}_W^{\mathrm{T}}, \tag{14}$$

where the impedance matrix $\boldsymbol{Z}_W$ is:

$$\boldsymbol{Z}_W = \mathbf{W}\left(j\omega\mathbf{M} + \mathrm{diag}(\mathbf{R})\right)\mathbf{W}^{\mathrm{T}}. \tag{15}$$

In our notation, the operator $\mathrm{diag}(\mathbf{X})$ takes a row vector $\mathbf{X}$ and creates a square matrix where $\mathbf{X}$ is put on the main diagonal and all other elements in the square matrix are equal to zero. Equation (15) can be rewritten as:

$$\boldsymbol{Y}_W\left(\boldsymbol{V}_W^{\mathrm{T}} - \mathrm{diag}\left(j\boldsymbol{X}_{C_W}\right)\mathbf{I}_W^{\mathrm{T}}\right) = \mathbf{I}_W^{\mathrm{T}}, \tag{16}$$

where $\boldsymbol{Y}_W = \boldsymbol{Z}_W^{-1}$. Note that from (10) – (13) only the first two elements of the row vector $\left(\boldsymbol{V}_W^{\mathrm{T}} - \mathrm{diag}\left(j\boldsymbol{X}_{C_W}\right)\mathbf{I}_W^{\mathrm{T}}\right)$ on the left-hand side of (16) are non-zero. With this insight, we extract the following 2×2 matrix equation from (16):

$$\begin{bmatrix} Y_{W,11} & Y_{W,12} \\ Y_{W,21} & Y_{W,22} \end{bmatrix}\begin{bmatrix} V_{in} + j\dfrac{I_p}{\omega C_p} \\ V_{rect} + j\dfrac{I_s}{\omega C_s} \end{bmatrix} = \begin{bmatrix} I_p \\ I_s \end{bmatrix}, \tag{17}$$

Equation (17) can be rewritten as:

$$\begin{bmatrix} V_{in} \\ V_{rect} \end{bmatrix} = \begin{bmatrix} Z'_{W,11} - j\dfrac{1}{\omega C_p} & Z'_{W,12} \\ Z'_{W,21} & Z'_{W,22} - j\dfrac{1}{\omega C_s} \end{bmatrix}\begin{bmatrix} I_p \\ I_s \end{bmatrix}, \tag{18}$$

where the impedance parameters $Z'_{W,11}$, $Z'_{W,12}$, $Z'_{W,21}$, $Z'_{W,22}$ are computed by the inverse equation:

$$\begin{bmatrix} Z'_{W,11} & Z'_{W,12} \\ Z'_{W,21} & Z'_{W,21} \end{bmatrix} = \begin{bmatrix} Y_{W,11} & Y_{W,12} \\ Y_{W,21} & Y_{W,22} \end{bmatrix}^{-1}. \tag{19}$$

From (18) we chose the values of the compensation capacitors that cancel the reactive components of the impedance terms $Z'_{W,11}$ and $Z'_{W,22}$:

$$C_p = \frac{1}{\omega \mathrm{Im}\left[\mathrm{Z}'_{W,11}\right]}, \tag{20}$$

$$C_s = \frac{1}{\omega \mathrm{Im}\left[\mathrm{Z}'_{W,22}\right]}. \tag{21}$$

We obtain $\boldsymbol{X}_{C_W}$ by substituting (20) and (21) into (13). Next, substituting (20) and (21) into (18) yields Fig. 6 – 8 present flux density plots generated by FEMM for each optimized shielding configuration under consideration. The results shows that the active cancellation loop is the most compact in terms of radius and most effective at cancelling the leakage field over a wide area. However, the active cancellation coil has two main disadvantages. First, it requires placement at z-postions below the primary coil (i.e., underground) to achieve optimal leakage cancellation, and second, the current magnitude through this coil is high, since it is equal to the current through the primary. This adds additional loss and requires a bulky Litz wire to support the high current. In comparison, the passive cancellation loops can suppress the EMF emission with much lower current, and can therefore be implemented with lower-profile Litz wires.

$$\begin{bmatrix} V_{in} \\ V'_{bat} \end{bmatrix} = \begin{bmatrix} \mathrm{Re}\left[Z'_{W,11}\right] & Z'_{W,12} \\ Z'_{W,21} & \mathrm{Re}\left[Z'_{W,22}\right] \end{bmatrix}\begin{bmatrix} I_p \\ I_s \end{bmatrix}. \tag{22}$$

Solving (22) for V_{in} in terms of the known secondary voltage $V'_{bat} = 4V_{bat}/\pi$ and current $I_s = -2\,P_{bat}/V'_{bat}$ yields:

$$V_{in} = \left(\frac{\mathrm{Re}\left[\mathrm{Z}'_{W,11}\right]}{\mathrm{Z}'_{W,12}}\right)\left(V'_{bat} - I_s\mathrm{Re}\left[\mathrm{Z}'_{W,22}\right]\right) + I_s\mathrm{Z}'_{W,12} \tag{23}$$

Substituting (23) into (8) yields a solution for $\boldsymbol{V}_W$. Next we substitute $\boldsymbol{V}_W$ and $\boldsymbol{X}_{C_W}$ into (14) and solve for $\mathbf{I}_W$. Finally, we solve for $\mathbf{I}$ by substituting $\mathbf{I}_W$ into (12).

The leakage magnetic B-field at position $P(r, z)$ is found with the aid of (2) and (3) by computing:

$$B_P = \sqrt{\left|\widehat{\mathbf{B}}_r\mathbf{I}^{\mathrm{T}}\right|^2 + \left|\widehat{\mathbf{B}}_z\mathbf{I}^{\mathrm{T}}\right|^2}. \tag{24}$$

If we ignore proximity effects, the total Litz wire conduction loss $P_{l,wire}$ is found with the aid of (6) by computing:

$$P_{l,wire} = \frac{1}{2}\mathbf{I}\mathrm{diag}(\mathbf{R})\mathbf{I}^{\mathrm{H}}, \tag{25}$$

where $\mathbf{I}^{\mathrm{H}}$ is the conjugate transpose of $\mathbf{I}$. The coil-to-coil power transfer efficiency η is given by the expression:

$$\eta = \frac{P_{bat}}{P_{l,wire} + P_{l,core} + P_{l,plate} + P_{bat}}, \tag{26}$$

where $P_{l,core}$ is the power loss in the ferrite core and $P_{l,plate}$ is the loss due to eddy currents induced in the aluminum plates. The values of $P_{l,core}$ and $P_{l,plate}$ can be found via a second FEA with FEMM by driving the coils with the known current values (obtained from the solution of $\mathbf{I}$) and computing losses using numerical volume integrations and known material properties.

III. Results

For the three shield types illustrated in Fig. 3 our goal is to find the optimal vertical positions z_c and radii r_c of each individual turn to minimize flux at $P(r, z) =$ (800 mm, 75 mm). Table II presents the results for different numbers of turns: $N_C = 1, 2,$ and 3. The simulation-based optimization was performed using FEA with FEMM to analyze the magnetic

TABLE II
SIMULATION-BASED OPTIMIZATION RESULTS

Shield description	Plot	η (%)	B_P (μT_{rms})	Winding currents (A_{rms})	z-postions and radii (z_c, r_c) of wndings (mm)
No shield	Fig. 4 (b)	99.4	25.63	NA	NA
Type 1: Passive loops. ($N_c = 1$).	Fig. 6 (a)	99.4	3.50	c_1: 12.00	c_1: (0, 745)
Type 1: Passive loops. ($N_c = 2$).	Fig. 6 (b)	99.4	2.00	c_1: 7.65 c_2: 6.34	c_1: (0, 739) c_2: (0, 749)
Type 1: Passive loops. ($N_c = 3$).	Fig. 6 (c)	99.4	0.82	c_1: 6.90 c_2: 1.36 c_3: 6.21	c_1: (0, 735) c_2: (0, 741) c_3: (-1, 746)
Type II: Passive coil. ($N_c = 2$).	Fig. 7 (a)	99.4	0.50	c_1: 7.63 c_2: 7.63	c_1: (0, 725) c_2: (0, 740)
Type II: Passive coil. ($N_c = 3$).	Fig. 7 (b)	99.4	0.50	c_1: 5.35 c_2: 5.35 c_3: 5.35	c_1: (0, 721) c_2: (0, 726) c_3: (0, 739)
Type III: Active coil. ($N_c = 1$).	Fig. 8 (a)	99.3	1.58	c_1: 50.57	c_1: (-60, 608)
Type III: Active coil. ($N_c = 2$).	Fig. 8 (b)	99.3	1.55	c_1: 51.70 c_2: 51.70	c_1: (-158, 500) c_2: (-18, 528)
Type III: Active coil. ($N_c = 3$).	Fig. 8 (c)	99.2	1.54	c_1: 53.00 c_2: 53.00 c_3: 53.00	c_1: (-188, 373) c_2: (-169, 400) c_3: (-18, 528)

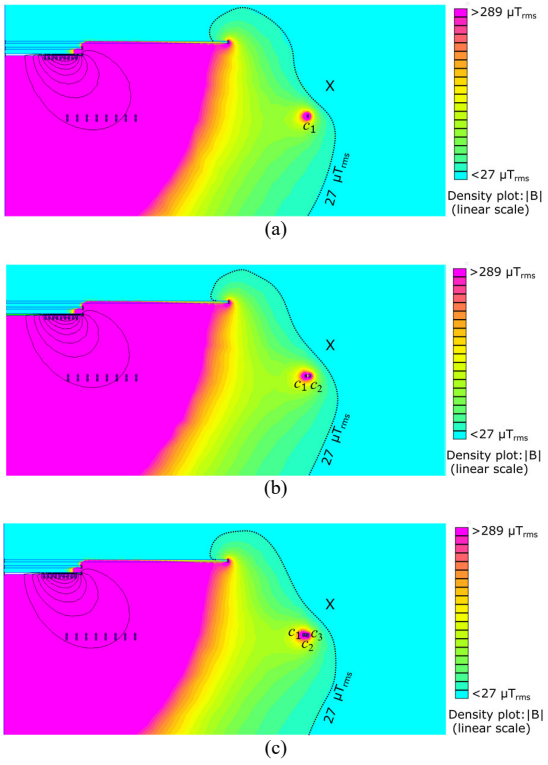

Fig. 6. Type I: Flux density plots showing shielding effectiveness of an optimized passive cancellation loop array: (a) N_C=1, (b) N_C=2, and (c) N_C=3.

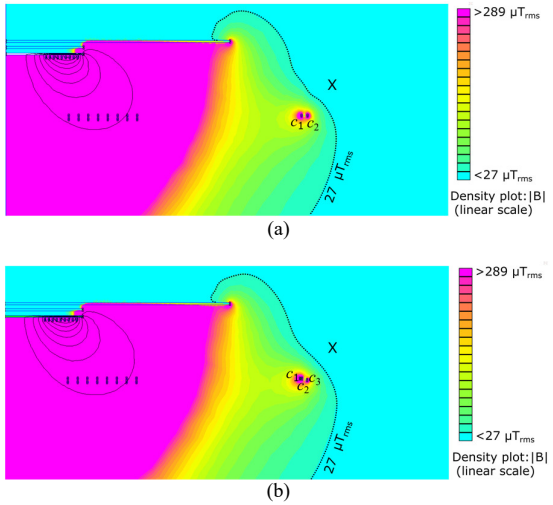

Fig. 7. Type II: Flux density plots showing shielding effectiveness of an optimized passive cancellation loop array: (a) N_C=2 and (b) N_C=3. Note that the flux density plot for the Type II N_C=1 case is equivalent to that of the Type I N_C=1 case shown in Fig. 6 (a).

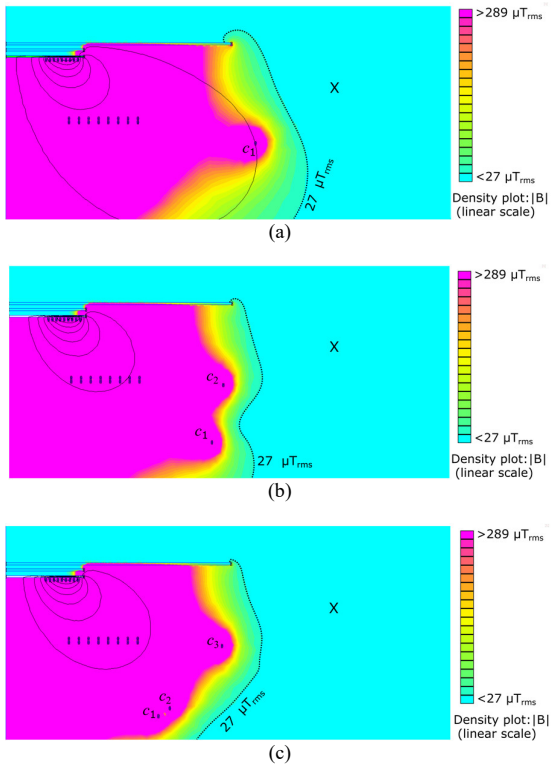

Fig. 8. Type III: Flux density plots showing shielding effectiveness of an optimized active cancellation loop array: (a) N_C=1, (b) N_C=2, and (c) N_C=3.

problem and MATLAB to implement a pattern search optimization algorithm. The optimization was performed with a constraint that the coil-to-coil power transfer efficiency η must not fall below 99%. The upper and lower bounds of $z_{c,i}$ and $r_{c,i}$ for each winding were set to $-400\ \text{mm} \leq z_{c,i} \leq 0$ and $5\ \text{mm} \leq r_{c,i} \leq 800\ \text{mm}$, respectively.

Another advantage of the passive shields is that they do not require an underground installation, since their optimal placement is generally on or very near the surface in the same z-position as the primary coil. The disadvantages of the passive cancellation loops are that they are less effective at cancellating the leakage field over a wide area and are less compact in that they require a larger radius.

Note that the values of η presented in Table II were calculated using (26). For this calculaton the core loss $P_{l,core}$ was evaluated using the known loss characteristics of Ferroxcube 3C95. The Litz wire loss $P_{l,wire}$ was calculated assuming a resistance of 592 mΩ/meter for the secondary and cancellation coils. For the primary coil, we assumed a resistance of 592/2 = 296 mΩ/meter to better match the SAE J2954 WPT3 ground assembly (GA) reference design which includes two Litz wires running in parallel.

IV. Summary and conclusions

In this work we performed simulation-based optimizations to compare and investigate the shielding effectiveness of three cancellation coil topologies. Our comparative analysis involved using FEA with FEMM and MATLAB to optimize the radii and vertical positions of the turns of the cancellation coils. We found that both passive configurations provided similar shielding performance, which was surprising as we anticipated the passive cancellation array would be clearly inferior to the coil. Both passive shields supported relatively low currents which makes possible the use of higher gauge Litz wire to reduce materials cost and weight. For all three cancellation coil topologies considered, only one turn is necessary for reducing the flux density well below 27 μT_{rms} at our measurement position at the side of the vehicle. Compared to the passive configurations, the active cancellation coil provides significantly better flux-cancellation over larger areas (e.g., compare Fig. 6 with Fig. 8) at the cost of carrying much higher currents. For future work, we indend to expand the scope of our comparative analysis by including capacitors in series with the passive cancellation coils.

Acknowledgement

The authors would like to thank Dr. David Smith (ORNL), and Lee Slezak (U.S. Department of Energy) for their support and guidance on this work.

References

[1] A. A. S. Mohamed, A. A. Shaier, H. Metwally, and S. I. Selem, "A comprehensive overview of inductive pad in electric vehicles stationary charging," *Appl. Energy*, vol. 262, p. 114584, 2020.

[2] "J2954_201904 Wireless Power Transfer for Light-Duty Plug-in/Electric Vehicles and Alignment Methodology," 2019. [Online]. Available: https://doi.org/10.4271/J2954_201904.

[3] O. C. Onar, S. L. Campbell, L. E. Seiber, C. P. White, and M. Chinthavali, "A high-power wireless charging system development and integration for a Toyota RAV4 electric vehicle," in *2016 IEEE Transportation Electrification Conference and Expo (ITEC)*, 2016.

[4] D. Kim, S. Kim, S. Kim, J. Moon, I. Cho, and D. Ahn, "Coupling Extraction and Maximum Efficiency Tracking for Multiple Concurrent Transmitters in Dynamic Wireless Charging," *IEEE Trans. Power Electron.*, vol. 35, no. 8, pp. 7853–7862, 2020.

[5] A. Dayerizadeh, S. Taylor, H. Feng, and S. Lukic, "Light Weight and Efficient Litz-wire Based Ferrite-less Shielding for Wireless Power Transfer," in *2020 IEEE Applied Power Electronics Conference and Exposition (APEC)*, 2020.

[6] M. G. S. Pearce, M. J. O'Sullivan, C. Carretero, G. A. Covic, and J. T. Boys, "Optimising Ferrite-less Pad Reflection Winding with a Multi-Objective Genetic Algorithm," *2019 IEEE PELS Work. Emerg. Technol. Wirel. Power Transf. WoW 2019*, pp. 165–168, 2019.

[7] M. G. S. Pearce, G. A. Covic, and J. T. Boys, "Passive reflection winding for ferrite-less double D topology for roadway IPT applications," *2019 IEEE Energy Convers. Congr. Expo. ECCE 2019*, pp. 1202–1209, 2019.

[8] M. G. S. Pearce, G. A. Covic, and J. T. Boys, "Robust Ferrite-Less Double D Topology for Roadway IPT Applications," *IEEE Trans. Power Electron.*, vol. 34, no. 7, pp. 6062–6075, 2019.

[9] A. Tejeda, C. Carretero, J. T. Boys, and G. A. Covic, "Ferrite-Less Circular Pad with Controlled Flux Cancelation for EV Wireless Charging," *IEEE Trans. Power Electron.*, vol. 32, no. 11, pp. 8349–8359, 2017.

[10] Y. Takahashi, K. Hata, T. Imura, and Y. Hori, "Comparison of Capacitor- and Ferrite-Less 85kHz Self-Resonant Coils Considering Dielectric Loss for In-Motion Wireless Power Transfer," in *IECON 2018 - 44th Annual Conference of the IEEE Industrial Electronics Society*, pp. 5159–5163, 2018.

[11] M. Lu and K. D. T. Ngo, "Circuit Models and Fast Optimization of Litz Shield for Inductive-Power-Transfer Coils," *IEEE Trans. Power Electron.*, vol. 34, no. 5, pp. 4678–4688, 2019.

[12] M. Mohammad, M. S. Haque, and S. Choi, "A Litz-Wire Based Passive Shield Design to limit EMF Emission from Wireless Charging System," in *IEEE Energy Conversion Congress and Exposition (ECCE)*, 2018.

[13] D. C. Meeker, "Finite Element Method Magnetics (21Apr2019 Build)." [Online]. Available: https://www.femm.info/.

[14] T. Campi, S. Cruciani, F. Maradei, and M. Feliziani, "Magnetic field during wireless charging in an electric vehicle according to standard SAE J2954," *Energies*, vol. 12, no. 9, 2019.

[15] ICNIRP, "ICNIRP guidelines for limiting exposure to time-varying electric and magnetic fields (1 Hz to 100 kHz)," *Health Phys.*, vol. 99, no. 6, pp. 818–836, 2010.